The Bottom-Up Approach toward Artificial Optical Magnetism in Metastructures

Ashod Aradian, Philippe Barois, Olivier Mondain-Monval, Virginie Ponsinet, Alexandre Baron

▶ To cite this version:

Ashod Aradian, Philippe Barois, Olivier Mondain-Monval, Virginie Ponsinet, Alexandre Baron. The Bottom-Up Approach toward Artificial Optical Magnetism in Metastructures. Roberto Caputo; Giuseppe Emanuele Lio. Hybrid Flatland Metastructures, AIP Publishing, 2021, 978-0-7354-2287-2. ⟨10.1063/9780735422902_003⟩. ⟨hal-03375970⟩

HAL Id: hal-03375970
https://hal.science/hal-03375970v1

Submitted on 13 Oct 2021

The bottom-up approach towards artificial optical magnetism in metastructures

Ashod ARADIAN, Philippe BAROIS, Olivier MONDAIN-MONVAL, Virginie PONSINET and Alexandre BARON
Centre de Recherche Paul Pascal
CNRS – Bordeaux University
Pessac (France)

Abstract: The generation of artificial optical magnetism (AOM) in engineered composites has been the major concept that led to the emergence of the field of metamaterials at the turn of the millennium. Indeed, the proven possibility to manipulate the magnetic permeability of materials at microwave frequencies induced a considerable excitement in the scientific community as it opened the way to the design of unprecedented tools and devices for the control of light propagation. Extensions to higher frequencies of IR and visible light were soon proposed and tested by downsizing the artificial structures. The fabrication of negative index materials, optical cloaks or hyper-lenses seemed within reach. Two decades later, and after considerable research efforts, the applications of the AOM are still scarce and the concept seems to face a number of fundamental physical limits. We review in this chapter the state-of-the-art of the bottom-up approach whereby nanochemistry and colloidal physics are used to engineer hybrid metastructures exhibiting AOM in visible light or near IR.

1 - Introduction

Magnetic effects are notoriously negligible in natural materials at optical frequencies[1]. This paradigm was revisited in the last two decades with the emergence of metamaterials, artificial materials designed so as to generate a significant degree of magnetic polarization. The trick was to engineer a material made of a collection of resonant LC circuits of subwavelength size, which develop current loops[2]. The AOM concept was beautifully demonstrated at microwave frequencies in an artificial composite device combining split ring resonators (SRRs) and metallic wires[3,4]. Subsequently, a race towards higher frequencies started by reducing the size of the metallic resonators down to nanometer dimensions[5]. The fantastic capabilities of advanced top-down technologies enabled the realization of finely engineered nanostructures, designed so as to exhibit plasmonic resonances and optical magnetism. Several types of such devices operating in visible light or in the near infrared were successfully produced like metallic dimers[6,7], U-shaped imprints[8] or fishnet structures[9,10,11], in which AOM was reported and sometimes interpreted as producing negative values of the effective magnetic permeability and of the refractive index. In order to minimize optical losses, top-down technologies were also applied to silicon-based systems operating in the near infrared[12,13]. Mostly dedicated to surface patterning, top-down technologies do enable, sometimes, the fabrication of three-dimensional nanostructures of thickness comparable to the operating wavelengths[14,15,16]. Today, it is clear that AOM is an essential, if not necessary, ingredient for the development of metasurfaces.

This chapter focuses on the complementary bottom-up approach, whereby colloidal chemistry is used to synthesize the magnetic resonators. In contrast to top-down approaches, bottom-up fabrication often builds metamaterials in two steps, first synthesizing the basic building blocks (meta-atoms) that are subsequently assembled into a 2D or 3D material. Considering the huge number of nano-objects required, on the order of 10^8/mm² on a surface or 10^{12}/mm^3 in bulk, self-assembly appears as an efficient strategy for the realization of macroscopic materials. We review the most recent achievements of the bottom-up approach combining wet-chemistry and self-assembly for the generation of AOM, after outlining in section 2 the optical characterization techniques.

2 - Optical detection of AOM

2.1 – AOM detection in Meta-atoms

In the bottom-up approaches, meta-atoms usually consist in single nanoparticles or ensembles of nanoparticles arranged to exhibit a specific optical response (see examples in Section 3). The physical observables that characterize this response are contained in the scattering matrix of the system. For the sake of simplicity, we shall describe the characterization of isotropic systems, such that the scattering matrix is assumed to be diagonal with components S_1 and S_2. The components parallel (//) and orthogonal (⊥) to the scattering plane are expressed as:

$$\begin{pmatrix} E_{//} \\ E_{\perp} \end{pmatrix} \propto E_0 \begin{pmatrix} S_2(\theta) & 0 \\ 0 & S_1(\theta) \end{pmatrix} \begin{pmatrix} \cos\phi \\ \sin\phi \end{pmatrix}$$

with θ the scattering angle, ϕ the polarization angle and E_0 the incident field. The scattering coefficients can be expressed as a function of the Mie multipolar coefficients a_n and b_n[17]. From these, the extinction (σ_e), scattering (σ_s), and absorption cross-sections can be classically calculated[17].

Extinction spectra are usually retrieved by measuring the absorbance of a suspension of meta-atoms, using Beer's law. Alternatively, σ_e can be measured directly on a single particle by spatially modulating the position of the particle in the kHz range in the focal plane of a tightly focused light beam[18,19].

The scattering spectrum can be measured in several ways. At the single particle level, dark-field spectroscopy enables a measurement of the differential scattering cross-section integrated over the numerical aperture of the microscope objective used to collect the scattered light. Dark-field spectroscopy enables a qualitative comparison between experimental particles and numerical or theoretical designs, because the scattered signal is not altered by polydispersity.

Importantly, since the electric and magnetic responses of the meta-atom are carried by the a_n and b_n coefficients respectively, most techniques exposed thus far do not actually measure AOM directly, but rather the total scattering or extinction, i.e. a superposition of the fields radiated by magnetic and electric modes. Consequently, most of these optical characterizations usually require a theoretical or numerical model to interpret the spectral features of the measured quantities.

Another possibility for characterizing the scattering cross-section is to resort to polarization-resolved static light scattering spectroscopy (SLS) of suspensions of meta-atoms[20,21]. This enables a direct measurement of the differential scattering cross-section and has been used to characterize AOM (see Fig. 1). The differential scattering-cross section D_σ can be decomposed into two components, parallel and orthogonal to the scattering plane. Assuming the system to be purely dipolar, we may write at a scattering angle of 90°:

$$D_\sigma^{\perp}(90°) = \Lambda \cdot \frac{|S_1(90°)|^2}{k^2} = \Lambda \cdot \frac{9}{4k^2}|a_1|^2$$

$$D_\sigma^{//}(90°) = \Lambda \cdot \frac{|S_2(90°)|^2}{k^2} = \Lambda \cdot \frac{9}{4k^2}|b_1|^2$$

with k the wavevector and Λ an experimental (generally unknown) constant. Hence, electric and magnetic dipoles are obtained separately, and can be fully determined only if a reference is measured. However, the magnetic-to-electric ratio is always accessible[20,22,23,]:

$$R_{ME} = \frac{D_\sigma^{//}(90^\circ)}{D_\sigma^{\perp}(90^\circ)} = \frac{|b_1|^2}{|a_1|^2}$$

R_{ME} may be used as a figure of merit to maximize AOM with respect to the electric response of the meta-atom. When $R_{\mathrm{ME}} = 1$, the magnitude of the electric and magnetic dipoles are equal and the so-called Kerker regime is reached. The first Kerker condition is reached when $a_1 = b_1$ and ensures that the meta-atom is a purely forward-scattering dipole (zero back-scattering), also known as a Huygens dipole. The second Kerker condition is reached when $a_1 = -b_1$ and corresponds to a meta-atom that maximizes the backward scattering.

Under the condition that the meta-atoms remain dipolar and that the volume fraction of meta-atoms remains small enough, assembling meta-atoms with R_{ME} larger than 1 should produce metamaterials with $\mu > \varepsilon$, and $R_{\mathrm{ME}} = 1$ should produce a metamaterial with $\varepsilon = \mu$, that is, impedance-matched to free-space.

In the multipolar regime, $D_\sigma^{\perp}(90^\circ)$ and $D_\sigma^{//}(90^\circ)$ remain interesting observables as they enable distinguishing between even and odd-parity modes in the scattering:

$$D_\sigma^{\perp}(90^\circ) \propto \frac{|S_1(90^\circ)|^2}{k^2} = \frac{1}{k^2}\left[\frac{9}{4}|a_1|^2 + \frac{25}{4}|b_2|^2 + \cdots\right]$$

$$D_\sigma^{//}(90^\circ) \propto \frac{|S_2(90^\circ)|^2}{k^2} = \frac{1}{k^2}\left[\frac{9}{4}|b_1|^2 + \frac{25}{4}|a_2|^2 + \cdots\right]$$

They may be used to engineer specific scattering properties that depend on the interference of odd and even modes. For instance, the first generalized Kerker condition (GKC) occurs when the superposition of even modes is equal in amplitude and in phase to that of odd modes. Similarly to the dipolar case, this produces a situation where back-scattering is suppressed. Then, we have $D_\sigma^{\perp}(90^\circ) \sim D_\sigma^{//}(90^\circ)$. Though not exactly equivalent to the GKC, this approximation is a good indication toward an effective Huygens multipole[24].

Most experimental meta-atom results described in Section 3 follow one of the optical detection schemes of AOM exposed above.

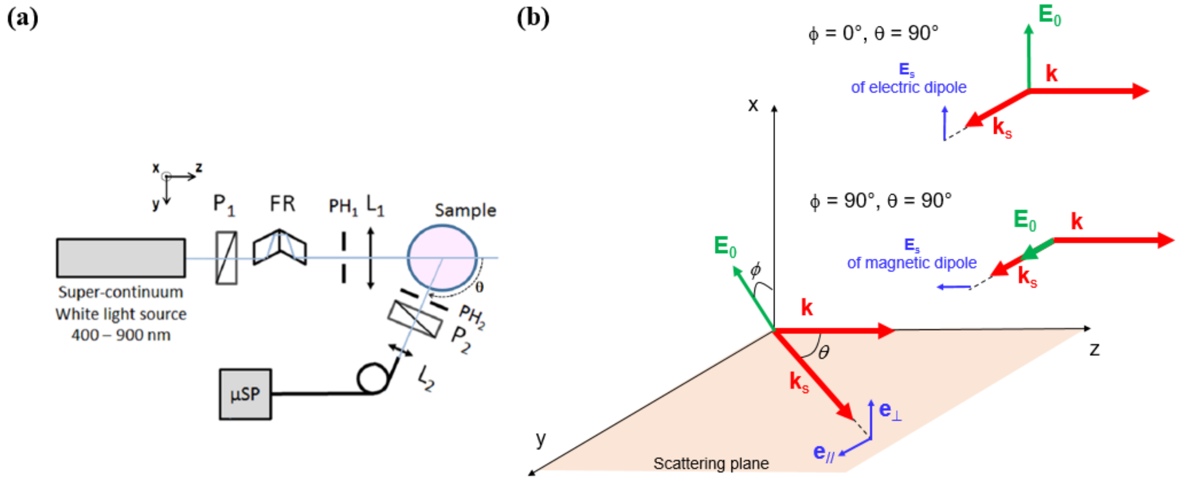

Figure 2.1: (a) Sketch of a polarization-resolved static light scattering setup (adapted from Ref.22 with permission from The Royal Society of Chemistry). It consists of two broadband polarizers (P_1 and P_2); a Fresnel rhomb tandem (FR); a focusing (L_1) and collection (L_2) lenses, two pinholes ($PH_{1,2}$) and a spectrometer (µSP). (b) Illustration of the vector fields involved in the illumination and

scattering. The incident electric field $\mathbf{E}_0$ is parallel to (O*xy*) and ϕ is the polarization angle with respect to (O*x*). The scattering plane (O*yz*) contains both $\mathbf{k}$ (incident wavevector) and $\mathbf{k}_s$ (scattered wavevector). The scattering angle θ is the angle between $\mathbf{k}$ and $\mathbf{k}_s$. In the scattering direction, the orthogonal ($\mathbf{e}_\perp$) and parallel ($\mathbf{e}_{//}$) components are represented. The top-right inset considers two specific situations where ($\phi = 0°$; $\theta = 90°$) and ($\phi = 90°$; $\theta = 90°$), which allow to separate the electric dipole contribution to the scattering from the magnetic dipole contribution.

2.2 – AOM in assembled metamaterials

From a suspension of meta-atoms synthesized to exhibit specific scattering properties, metastructures can be assembled, as two-dimensional metasurfaces (monolayers), structures with a few layers, up to bulk three-dimensional metamaterials. The characterization and measurement of electromagnetic constitutive properties, including artificial magnetism, is a difficult task where one should be wary of numerous pitfalls.

In principle, the most straightforward approach is to measure the complex reflection r and transmission t coefficients of a metastructure slab, to achieve some form of unambiguous determination of AOM, namely of $\mu(\lambda)$. This is hard experimentally in the optical range, but numerically straightforward: many metamaterial characterizations actually compute r and t through a rigorous full-wave simulation and retrieve both ε and μ in a first step, then comparing experimentally the measured reflectance $R = |r|^2$ and transmittance $T = |t|^2$ with those computed to justify indirectly the presence of artificial magnetism[25,26,27].
Alternatively, measuring ε and μ is equivalent to measuring the refractive index $n = (\varepsilon\mu)^{\frac{1}{2}}$ and the impedance $Z = (\mu/\varepsilon)^{\frac{1}{2}}$ of the metamaterial. Across a single interface between two materials, the reflection and transmission coefficients r_p, r_s, t_p, t_s for p- and s-polarized waves are expressed according to Fresnel's laws[28,29]: knowing the incident medium impedance Z_1, and the angles of incidence and refraction, a simple measurement of R and T is sufficient to find Z_2 in the metamaterial. The index of refraction of the metamaterial can be measured by resorting to interferometry using the field transmitted (or reflected) through a metamaterial slab of length small compared to the penetration depth in the metamaterial[30,31,32].

Finally, variable-angle spectroscopic ellipsometry can be used to measure AOM. Ellipsometry usually measures the complex ratio $\rho = r_p/r_s = \tan\psi\ e^{-i\Delta}$, where ψ and Δ are referred to as the ellipsometric angles. A first indirect measurement scheme consists in fitting $\psi(\lambda)$ and $\Delta(\lambda)$ assuming Lorentzian models for both ε and μ. This ensures that the optical parameters used for the spectral fitting are physical[6] and is well-suited to metamaterial slabs. In addition, Mueller-ellipsometry can provide access to permittivity, permeability, and chirality in thin nanostructures[33].

A strong word of caution is required here: despite abundant use in the literature, the above methods are of limited applicability for metastructures comprised of one or a few layers of resonators only. The extracted material parameters will depend on the angle of incidence, the slab thickness, and lose most of their predictive power for situations outside the measurement configuration[34,35,36,37].

One favorable case is a 3D, isotropic, semi-infinite metamaterial. Using spectroscopic ellipsometry, an analytical expression allows to obtain ε and μ from the experimental ratio ρ and the incidence angle θ_1, following a simple linear regression model:

$$Y = AX + B$$

with

$$Y = \left(\frac{1-\rho}{1+\rho}\right)^2 \frac{\sin^4\theta_1}{\cos^2\theta_1}$$
$$X = -\sin^2\theta_1$$
$$A = \left(\frac{\epsilon-\mu}{1-\epsilon\mu}\right)^2$$
$$B = A\epsilon\mu$$

ε is a solution to a second-order polynomial equation

$\epsilon^2 \pm \epsilon A^{\frac{1}{2}}\left(1-\frac{B}{A}\right) - B/A = 0$

And µ follows from

$$\epsilon\mu = n^2 = \frac{A}{B}$$

Imposing that the metamaterial be dissipative singles out the physical solutions and unambiguously determines both ε and μ[38,29]. The quality of this method is asserted by the quality of the linear regression and fails when spatial dispersion becomes important. In that case, the metamaterial can no longer be described by simply an electric permittivity and a magnetic permeability (see Section 4).

3: Synthetic meta-atoms for AOM:

Meta-atoms for AOM generation should exhibit a strong enough optical response, with dimensions noticeably shorter than the operating wavelengths to enable homogenization. For visible or near-IR light, dimensions should not exceed ~100nm typically. These two requirements are generally antinomic: small objects produce small optical effects. Optical resonators appear as the best opportunity to reconcile these two constraints, since resonances induce a significant amplification of the fields. Two classes of optical resonances are well known: plasmons, linked to the negative value of the dielectric permittivity in conductors, and Mie resonances which are cavity-type resonances mainly controlled by the morphology. Exploiting these natural resonances to induce an artificial magnetization requires specific designs[39], described below.

3-1- Plasmonic magnetic meta-atom:

3-1-1- Theoretical background:

Localized surface plasmon resonances (LSPR) occur in metallic nanoparticles, and the nature and size of the particle and surrounding materials determine their frequency. For instance, the resonance wavelengths are 550 nm and 440 nm for gold and silver nanoparticles of 10 nm-radius in water. Plasmonic resonances of metallic nanoparticles can trigger magnetization, when the particles are organized in nano-circuits, as suggested in early models illustrated in figure 3.1.a[40,41,42]. The circular plasmonic current generates the wanted local magnetization, which oscillates at the frequency of the light wave.

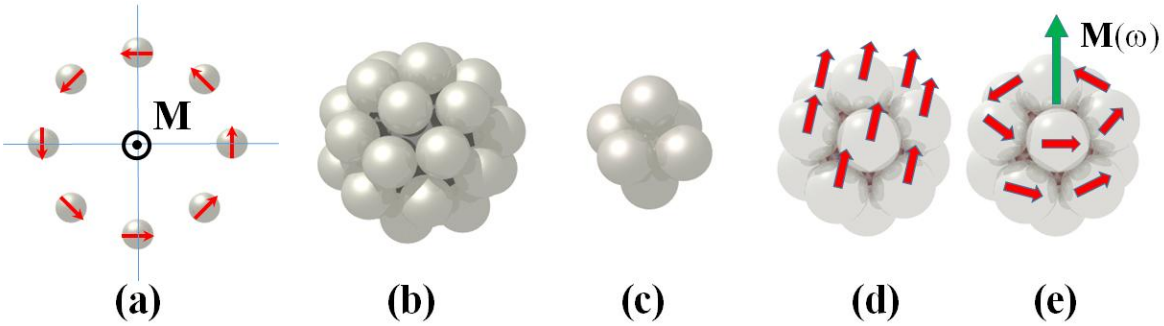

Figure 3.1: (a) Original model of plasmonic nano-ring[40]. (b) Raspberry-like magnetic nanocluster model[43] (c) Cube-based isotropic model[41]. (d-e) Sketches showing the plasmonic currents (red arrows) in the electric (d) and magnetic (e) resonant modes[44].

The plasmonic ring model has been further improved to promote an isotropic response of the magnetic meta-atoms by distributing the nanoparticles in a 3D symmetric cluster (figures 3.1.b-c). Metallic satellites are randomly distributed around a central dielectric core to form the so-called "plasmonic raspberry" nanostructure[43]. Fully ordered structures were also imagined by locating the metallic nanoparticles on the faces of a Platonic solid, e.g. six particles placed at the faces of a cube[41] (figure 3.1.c). In the example shown in figures 3.1.d-e, twelve silver satellites are located at the vertices of an icosahedron[44]. Numerical simulations reveal that the optical response of both the raspberry and icosahedral clusters is dominated by only three multipoles, namely the electric dipole (ED), the targeted magnetic dipole (MD), and the electric quadrupole (EQ) appearing at higher frequency. In computations on a bulk material made of a dense cubic lattice of such resonators, a sharp resonant behavior of μ_{eff} was found with extreme values reaching a few negative and positive units[43].

3-1-2- Experimental realizations: raspberry-like nanoclusters (R-NC)

The Simovski-Tretyakov model[43] of raspberry-like nano-clusters (R-NC) proved highly stimulating for nanochemists, who came up with many realizations summarized in Figure 3.2.

The basic strategy consists in attaching metallic nanoparticles (satellites) onto a dielectric nanosphere (core), self-assembled with the help of simple colloidal forces (i.e. electrostatic and Van der Waals) or more specific chemical bonds (after proper surface functionalization). Silica or polystyrene are commonly used for the core, gold or silver for the satellites. Although silver is preferable for its lower level of losses, gold satellites were often used as a proof of concept for their higher chemical stability and easier surface functionalization.

The first bottom-up realization of R-NCs is illustrated in figure 3.2.a-b[45]. 275 to 320 gold satellites of radius 10 ± 1nm are electrostatically assembled around silica cores of radius 130 ± 10nm. The extinction spectrum measured on a collection of such clusters (panel 3.2.b) exhibits a broad resonance at 670 nm, which is not present in the suspension of free satellites. This pioneering work reveals some features that will be found in all other systems: The sub-wavelength ratio, which we define as the outer diameter of the clusters divided by the resonant magnetic mode wavelength is hardly lower than 1.

Replacing gold by silver in the satellites gives the hope of a higher magnetic response for smaller clusters. Figure 3.2.c-d shows R-NCs made of a polystyrene core (D_{core} = 90nm) surrounded by about thirty silver satellites of diameter 36 nm attached by a thiol linker[20]. A fine scattering study of these silver R-NCs provided a direct identification of the magnetic dipolar response. Dark-field spectroscopy on a single R-NCs on the one hand, and polarized static light scattering on a population on the other hand, enabled to unambiguously distinguish the electric and magnetic scattering modes.

The next step in the characterization of AOM of R-NCs was obtained by measuring the magnetic-to-electric ratio across the whole visible spectrum in order to determine its maximum value and to localize the wavelength of the multipolar resonances. The polarized static light scattering method was implemented with a white light source, to study R-NCs made of 30nm gold[21] or 25nm silver satellites[38] around a 100nm-silica sphere (figures 3.2.e-g). The scattering cross sections recorded along the two principal output polarizations reveal two resonant features (figure 3.2.f and h). Numerical simulations confirm the contribution of only three significant modes in the visible spectrum, namely ED, MD and EQ in decreasing strength. For silver satellites, the magnetic-to-electric dipole ratio reaches the highest value $R_{ME} = 0.26$. Interestingly, the resonances of the three contributing modes largely overlap, which enables the simultaneous presence of electric and magnetic optical responses in the same wavelength range.

In an attempt to increase the magnetic optical response of the R-NC designs, Qian *et al.* investigated variations of the structural parameters by changing the core diameter and the size and number of metallic satellites[46]. Figures 3.2.i shows nanoclusters made of several layers of gold nanoparticles wrapping up the silica core. Experimental and simulated extinction spectra reveal dipolar resonances shifted towards the near IR domain (figure 3.2.j), while higher multipoles are present in the visible.

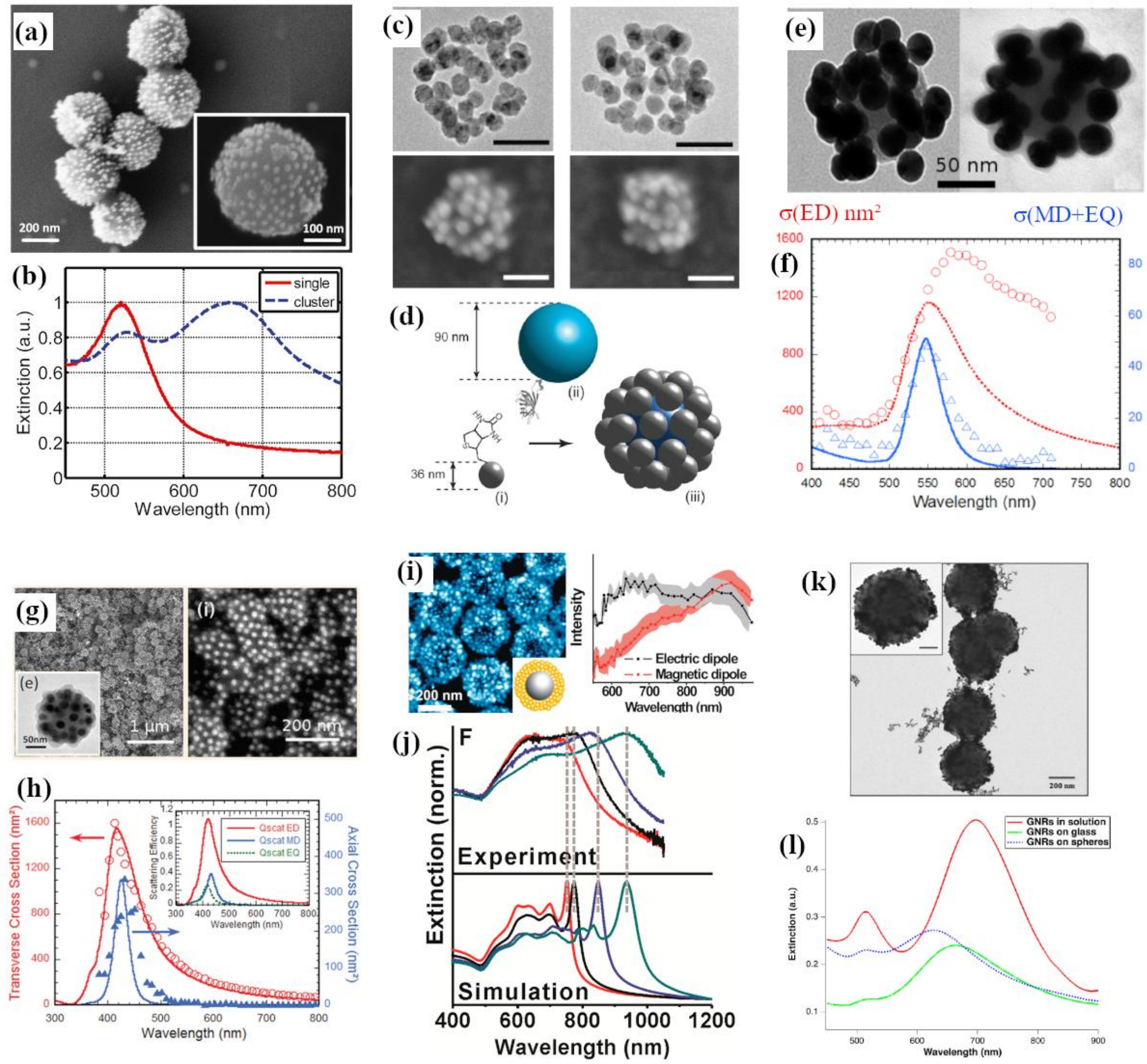

Figure 3.2: Raspberry-like magnetic nanoclusters (R-NCs). (a) SEM picture of gold-on-silica R-NCs. (b) Extinction spectrum showing the magnetic resonance at 680 nm (Reprinted with permission from

Ref.[45]. Copyright 2011 American Chemical Society). (c) TEM (top) and SEM (bottom) images of clusters of silver nanospheres covalently attached to a polystyrene core as shown in (d) (Reprinted with permission from Ref.[20]. Copyright 2013 American Chemical Society). (e) TEM micrographs of gold-on-core R-NCs. (f) Plots of the orthogonal (red) and parallel (blue) scattering corresponding mainly to the electric dipole and magnetic dipole contributions (Reprinted with permission from Ref.[21]. Copyright 2015 by the American Physical Society.). (g-h) similar to (e-f) with silver satellites. Inset in (h) shows the strength of the three scattering modes, ED, MD and EQ (Reproduced from Ref.[38] with permission from The Royal Society of Chemistry) (i) R-NCs with a thicker layer of gold satellites. (j) Experimental (top) and simulated (bottom) extinction spectra showing the first dipolar resonances in the near IR (Reprinted with permission from Ref.[46]. Copyright 2015 American Chemical Society). (k) TEM micrographs of clusters made of gold nanorods attached on silica microspheres. (l) Extinction spectra revealing the electromagnetic couplings of the nanorods in an assembled surface (Reprinted with permission from Ref.[47]. Copyright 2020 American Chemical Society).

Replacing the spherical satellites by metallic nano-rods provides also an interesting structural option as it enables some tuning of the resonance frequency by simply adjusting the aspect ratio of the nano-rods[47]. Note that magnetic dipoles based on plasmonic current loops were also observed in colloidal nanoarchitectures on surfaces[48,49].

3-1-2- Experimental realizations: Platonic nanoclusters (P-NC)

The perfect organization of a well-defined number of metallic satellites on the faces of a Platonic solid is a smart way to produce clusters with isotropic optical properties. Figure 3.1.c shows the example of a cluster made of six identical spheres sitting on the vertices of an octahedron. It is remarkable that bottom-up synthetic methods not only can produce random organization of the satellites as in the R-NC model, but also such quasi-perfect platonic-like nanoclusters (P-NCs) with a large-scale output.

In figure 3.3.a, gold nanospheres are attached to thiol groups at predefined locations on the surface of a genetically engineered cowpea mosaic virus with icosahedral symmetry[50]. Optical resonances are observed in the visible, with a 10-fold enhancement of the local field. The next examples are based on the concept of “patchy” particles whereby well-defined areas of a core nanoparticle are decorated with specific chemical functions, which will subsequently be used to attach or grow the metallic satellites[51]. Figure 3.3.b. illustrates the multistep “patchy” particle strategy and a remarkable set of P-NCs of tetrahedral, octahedral and icosahedral symmetry[52].

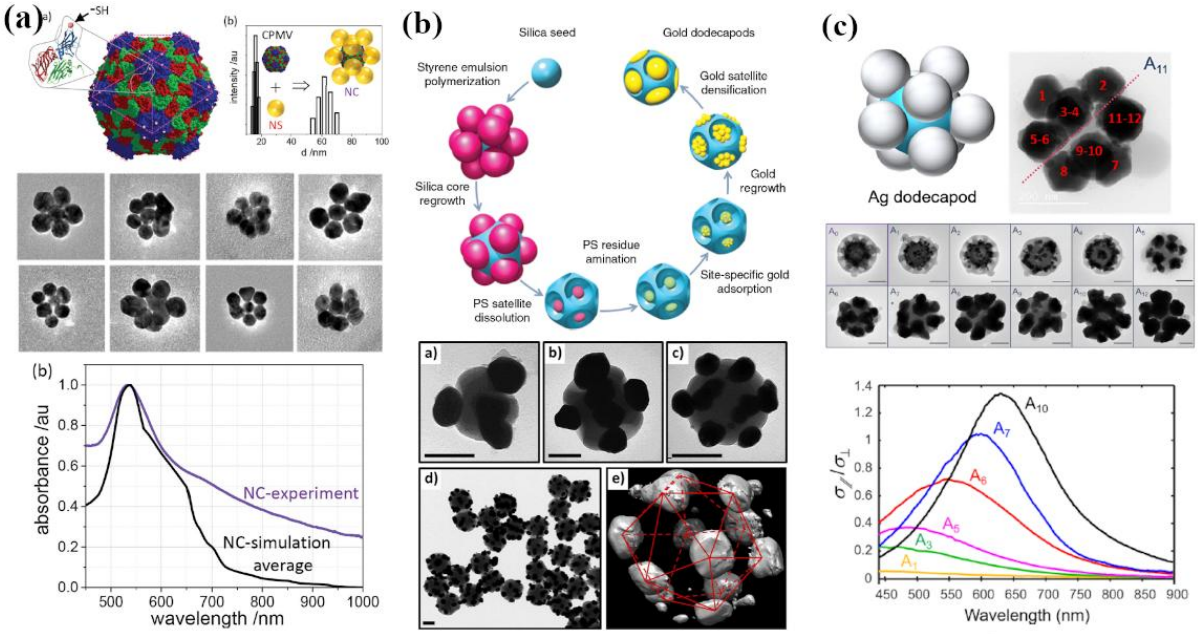

Figure 3.3: Platonic nano-clusters (P-NCs) (a) Virus model and TEM picture of P-NCs with 30nm-silver satellites (top). Normalized absorbance spectra comparing the experimental (purple) and averaged simulation (black) (bottom) (Reproduced from Ref.[50] with permission). (b) Schematic process for the synthesis of gold dodecapods).(top) (Reprinted with permission from Ref.[23]).Transmission electron micrographs of silica/gold P-NCs four, six or twelve satellites (scale bars 100 nm) and 3-D reconstruction of a dodecapod obtained by electron tomography (bottom) (Reprinted with permission from Ref.[52]), (c) scheme and TEM images of a dodecapod and the steps of silver satellite growth (scale bars 100 nm) (top) and spectral variation of the magnetic-to-electric ratio along the satellite growth (bottom) (Adapted with permission from Ref. [24] . Copyright 2021 American Chemical Society).

An optical study of gold dodecapods of icosahedral symmetry revealed a magnetic-to-electric ratio of the dipolar scattering of 0.15, well above the value 0.045 obtained for the R-NC form of equivalent size and gold amount[23]. The same “patchy particle” strategy was used with silver satellites to further enhance the AOM[24]. Figure 3.3.c presents a series of silver dodecapods of increasing satellite size preserving the icosahedral symmetry. The polarized scattering study (bottom) shows that the parallel-to-transverse scattering ratio $D_{\sigma}^{//}(90°)/D_{\sigma}^{\perp}(90°)$ increases with the amount of silver to reach a record value higher than 1, definitely higher than the value 0.28 obtained for silver R-NCs of similar size. The numerical multipole analysis indicates that the generalized Kerker condition is fully or nearly satisfied across the visible range, which is confirmed experimentally by an angular scattering study evidencing a strongly dominant forward scattering: these resonators are examples of Huygens multipoles as described in section 2.1.

3-2- Dielectric Mie-resonant magnetic meta-atom:

The advantage of Mie-resonant particles made of transparent dielectrics has been long recognized for the reduction of optical losses[53,54]. Upon increasing frequency, the two dipolar resonances of the Mie expansion appear first. For a sphere of refractive index *n*, the magnetic resonance, naturally of interest for the AOM quest, occurs for a wavelength $\lambda = \lambda_0/n$ close to the diameter *D*. The additional requirement of sub-wavelength size $D << \lambda_0$ implies the search of transparent materials of high refractive index. Available high-index materials are shown in figure 3.4.a: the highest possible values do not exceed 4 to 5. Bottom up approaches have investigated two materials, titanium dioxide (TiO_2) with an index of 2.6 and crystalline silicon that has an index close to 4 (Fig. 3.4.b)[55]. Amorphous silicon is less desirable for its higher absorption coefficient *k*. TiO_2 nano and microparticles can be produced by sol-gel chemistry, but the effective refractive index of the particles is generally disappointing, about 1.6 instead of 2.6 for the anatase crystalline phase. Synthesizing crystalline silicon (c-Si) nanospheres is more challenging, but more rewarding.

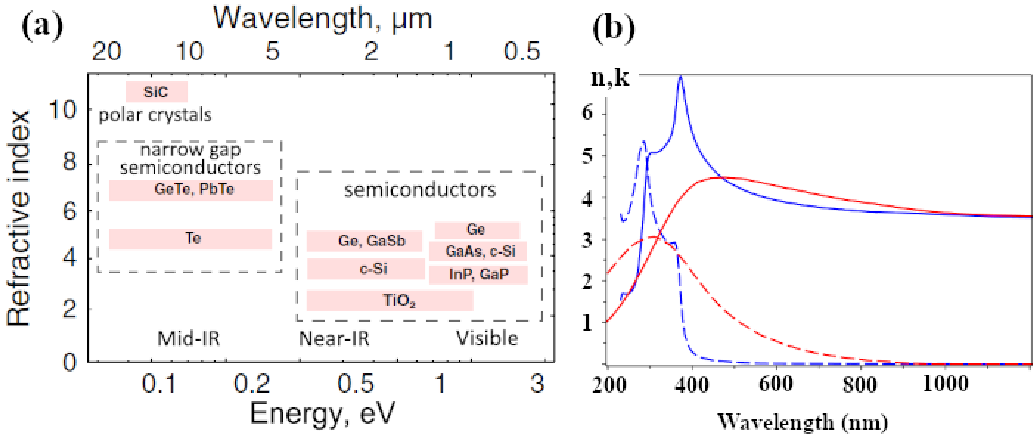

Figure 3.4: (a) Refractive indices of materials available for dielectric nanophotonics from visible to mid-IR spectral ranges (Reprinted with permission from Ref. 54. © The Optical Society). (b) Optical index[55] of crystalline (blue) and amorphous (red) silicon. Solid (dashed) lines represent real (imaginary) part.

Si nanospheres have been produced by laser ablation of Si[56] or silicon-on-insulator targets[57], collected on a glass slide, laser-recrystallized and optically characterized by dark field optical microscopy. Their dipolar magnetic and electric Mie resonances in the visible are found in full agreement with the Mie theory (Fig. 3.5).

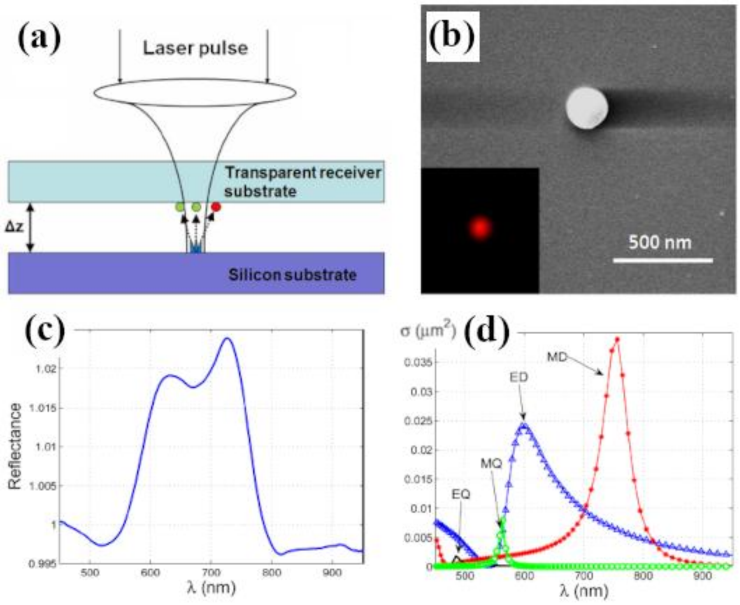

Figure 3.5. (a) Schematic presentation of laser induced production of silicon nanospheres. (b) SEM image of a Si sphere of radius R = 104 nm. Inset shows the corresponding dark-field images. (c)

Experimental reflectance spectrum of the 104 nm-nanoparticles located on a glass substrate. (e) contributions of the different multipoles to the calculated scattering cross sections. (Reprinted with permission from Ref. 56. Copyright 2012. American Chemical Society.)

The laser ablation is undoubtedly excellent to produce perfectly calibrated c-Si nanospheres, though in limited amount. On the other hand, the mass-production of silicon nano-spheres of well-controlled size and internal structure by chemical synthesis from a silicon-rich precursor is a tough challenge[58]: Figures 3.6.a-b illustrate two recent chemical paths based on solvo-thermal synthesis[59] and thermal decomposition[60] of various silane precursors.

Interestingly, a large-scale and low-cost production of crystalline, spheroidal silicon nanoparticles (100-200nm) exhibiting magnetic dipolar scattering in the visible was obtained by physically grinding silicon lumps in a kitchen blender[61] (fig. 3.6.c).

More recently, perfectly spherical crystalline silicon was produced from silicon oxide (SiO) lumps, annealed at high temperature to induce spherical Si inclusions, which are then extracted and size-sorted by centrifugation[62] (figure 3.6.d). Their magnetic dipolar resonance was observed throughout the visible for diameters ranging from 90 to 200 nm.

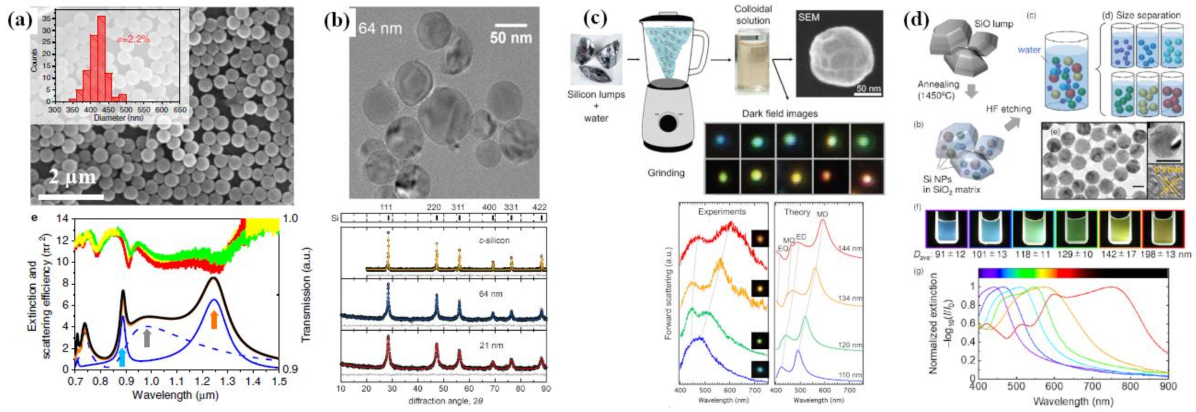

Figure 3.6. (a) SEM picture of silicon nanospheres made by solvothermal synthesis from a trisilane precursor (top). Extinction spectrum revealing the magnetic and electric dipoles in the infrared (bottom) (Reprinted by permission from Nature Publisher from Ref.[59]. Copyright 2013). (b) Silicon nanospheres synthesized from Hydrogen Silsesquioxane precursor (top). X-ray diffraction diagrams evidencing the crystalline structure (bottom) (Reprinted with permission from Ref.[60] Copyright (2019) American Chemical Society). (c) Kitchen-blender fabrication of crystalline silicon spheroids (top). Scattering spectra showing the size-dependent electric and magnetic dipolar resonances (bottom) (Reprinted with permission from Ref.[61]. Copyright (2019) American Chemical Society). (d) Crystalline silicon nanospheres produced by thermal annealing and etching of SiO lumps (top). Extinction spectra showing the two dipolar resonances (bottom) (Reprinted with permission from Ref.[62]. Copyright (2020) American Chemical Society).

In the above examples, the electric and magnetic dipolar resonances occur at different wavelengths, in agreement with the Mie-theory for high-index spheres. Merging these two resonances is desirable to produce broad-band Huygens’ sources with applications to perfect absorption[63]. Coating a silicon core with a dielectric shell allows controlling the relative frequencies of the two dipolar resonances[64], as was experimentally demonstrated on Si particles made by laser ablation and subsequently oxidized to grow a silica shell[65]. The mass-production of similar core-shell structures was made possible[66] by adapting the solvo-thermal synthesis (Figure 3.7.a-b). Dark-field studies evidenced the full overlap of the electric and magnetic dipole resonances with equal strength (Fig. 3.7.c). Numerical simulations show that the electric and magnetic dipoles are located respectively in the shell and in the core (Fig. 3.7.d).

These last works[61,62,66] announce the upcoming large-scale availability of crystalline silicon nanospheres, which opens the way to future applications of AOM in metasurfaces or metamaterials.

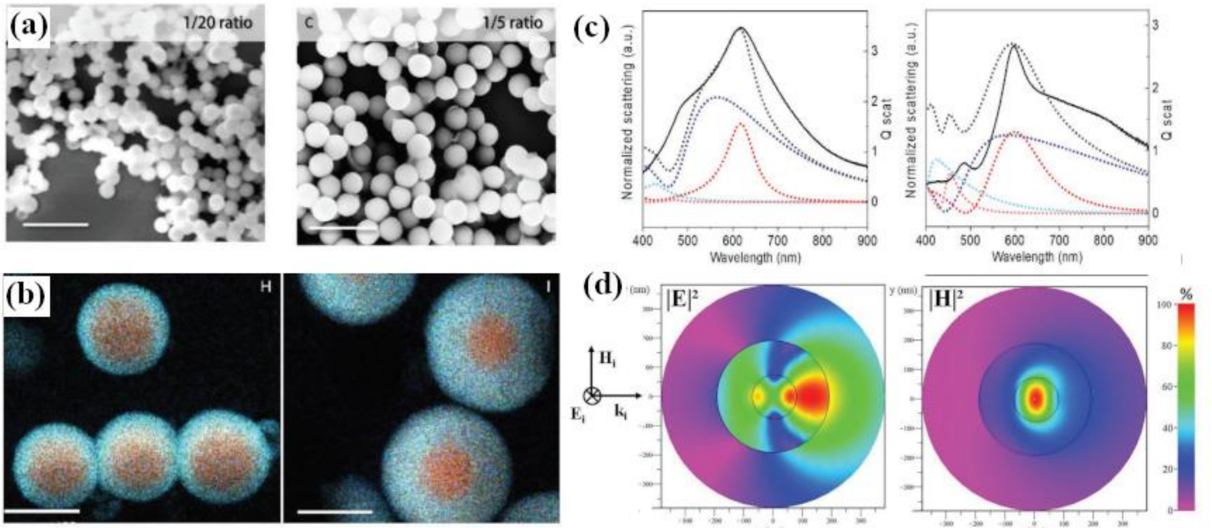

Figure 3.7. (a) SEM micrographs of silicon nanospheres made by solvothermal synthesis from two different mixtures of trisilane and bis-amidinate precursors (bar = 1µm). (b) STEM-EDX elemental analysis evidencing the core-shell structure Si@SiO$_x$N$_y$ (bar = 200nm). (c) Experimental (solid line) and simulated (dots) dark-field spectra showing the overlapping electric (blue) and magnetic (red) dipolar scattering. (d) Electric (left) and magnetic (right) field maps. (Reprinted from Ref.[66] with permission from Wiley and Sons Publisher).

3-3- Plasmon-assisted Mie-resonators:

The choice of high-index dielectrics is limited in visible light (Figure 3.4.a), and even more so for nanochemistry synthetic approaches. An alternative consists in using the plasmonic resonance of a metal-dielectric composite to generate an effective material with a high effective index, which itself is subsequently shaped in spheres subject to Mie resonances[67]. This hierarchical approach was realized using small crosslinkers between particles to produce quasispherical aggregates, inducing a magnetic mode visible in the extinction spectra for large enough nanoparticles (20 nm)[68]. More monodisperse clusters were targeted with emulsion processes. Figures 3.8.b-d show spherical clusters of silver nanoparticles encapsulated in oil-in-water emulsions and aggregated by dithiol linkers[69], which display dipolar Mie resonances in extinction spectra. Figures 3.8.e-g show clusters of gold nanoparticles synthesized in a water-in-oil emulsion, where water evaporation confines the nanoparticles into controlled aggregates, which were shown to have a strong magnetic dipolar resonance[22].

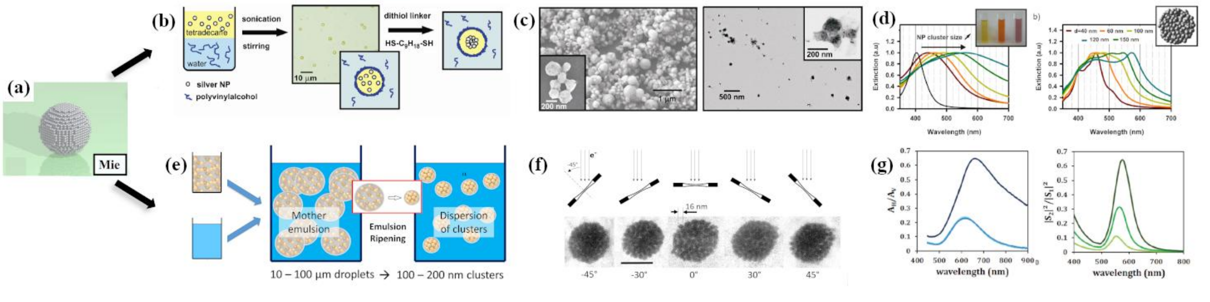

Figure 3.8: (a) Hierarchical model of a Mie-resonant sphere made of an artificial Lorentz-resonant high-index material (Reprinted with permission from Ref.[67] Copyright (2007) by the American Physical Society). (b-d) Realization by silver nanoparticles aggregation in an oil-in-water emulsion (c) SEM images of the raw emulsion showing the polymeric nanocapsules (left) and TEM images of the NP-clusters (right) (d) Extinction measurements and simulations showing the magnetic resonance. (b-c-d reprinted with permission from Ref 69 © The Optical Society.) (e-g) Realization of spherical gold clusters by drying a water-in-oil emulsion. (f) Cryo-TEM images recorded at different angles proving the spherical shape of the clusters. Scale bar is 100 nm (g) Measurements (left) and simulations (right) of the magnetic-to-electric dipolar ratio. (e-f-g reprinted from Ref.[22] with permission from The Royal Society of Chemistry).

These emulsion processes are efficient and cost-effective for a large-scale production of resonators in a solvent. Moreover, numerical simulations[70] and measurements[22] show that their optical properties can be finely tuned via structure control.

3-4- Conclusion:

This section shows that bottom-up approaches offer a large variety of AOM meta-atoms. In many cases, the magnetic response is of the same order as the electric one, opening the way for efficient Huygens' source production for forward-only scattering. The size of the magnetic meta-atom is mostly in the 100-200 nm range, only moderately sub-wavelength for visible-light applications, and often polydisperse. Optical applications may require post-synthesis size-sorting for a finer control of the properties. Tunability was demonstrated, and the tool-box of the classical colloidal physical-chemistry offers the variability for exploring resonance engineering.

-4- Self-assembled materials

4 – 1 – 2D assemblies, metasurfaces:

AOM studies in metasurfaces fabricated by self-assembly are scarce, compared to the abundant literature dealing with the top-down approach[71], more powerful indeed for a perfect surface ordering of meta-atoms. Nevertheless, self-assembly can for example produce an excellent organization of spheres of uniform diameter on a substrate[59] (see Figure 4.1a): a hundred percent transmission band is found in experiments and FDTD numerical simulations in the near IR, and attributed to impedance-matching caused by both the magnetic and the electric dipole interactions.

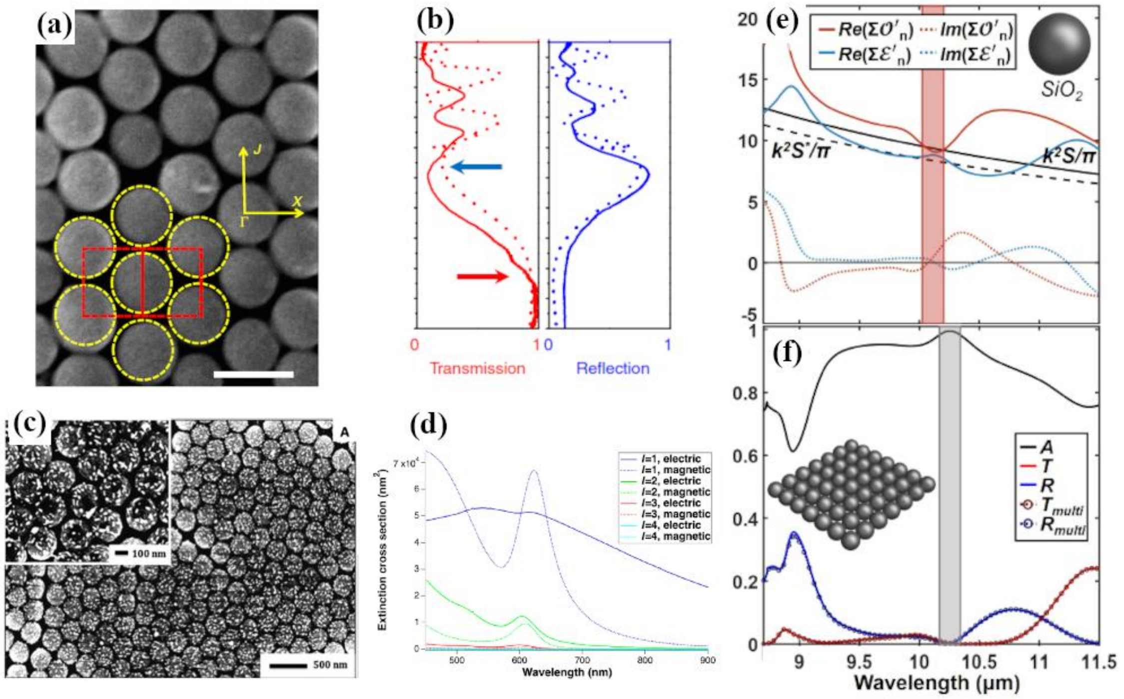

Figure 4.1: (a-b) 2D photonic crystal of silicon microspheres (a) SEM image (scale bar, 500 nm). (b) Transmission (red) and reflection (blue) spectra at normal incidence obtained from the experiment (solid lines) and the FDTD simulation (dotted lines) (Reprinted by permission from Nature Publisher from Ref.[59]. Copyright 2013)). (c-d) Array of silica microspheres decorated with gold nanorods (c) SEM micrograph. (d) Computed contribution of the different multipole moments to the extinction spectra for an isolated cluster. (Reprinted with permission from Ref.[47]. Copyright 2020 American Chemical Society) (e-f) Design of a perfect absorber using the multipolar behavior of individual meta-atoms. (e) Wavelength dependence of the sum of even and odd multipole coefficients of a single SiO2 microsphere in vacuum (D=4.3µm) (f) Spectra of R, T and A calculated for an infinite square array of SiO_2 microspheres with a surface fill fraction of 0.7. (Reprinted with permission from Ref. 63 © The Optical Society.)

Interestingly, a monolayer of R-NCs can be prepared in two steps[47] by adsorbing the metallic satellites onto the previously deposited regular array of dielectric spheres. Figure 4.1d shows a triangular lattice of silica beads decorated with gold nanorods. The extinction spectrum of the array (Fig. 3.2.l) is consistent with the presence of magnetic multipoles as shown by numerical simulations in figures 4.1e.

The design of the meta-atoms can actually be adjusted in numerical simulations to promote perfect reflection, transmission or absorption. In this latter case, two conditions should be met simultaneously, namely the extinction of the reflected wave (generalized Kerker's condition) and a π-phase shift of the transmitted wave for destructive interference with the incident light[63]. Figures 4.1g-h show an example of a 2D array of meta-atoms made of 13 spheres of germanium of 75 nm radius producing perfect absorption in the visible at a wavelength of 790 nm. In this study, numerical simulations point out the significant contribution of scattering multipoles for each meta-atom, and the importance of the inter-particle coupling in the array. Reducing the AOM to the effect of the sole magnetic dipole would be insufficient.

Very few experimental examples of self-assembled metasurfaces operating in visible light have been reported so far, but the recent availability of a large number of magnetic meta-atoms should enable and stimulate new realizations. Several self-assembly techniques are commonly available to deposit nanoparticles on a substrate like spin-coating[72], dip-coating[73], blade-coating[74] or Langmuir-Blodgett transfer[75,76].

4 – 2 – 3D assemblies: bulk magnetic metamaterials

The ability of the bottom-up route to synthesize a huge number of magnetic meta-atoms enables bulk metamaterials fabrication. Figure 4.2 illustrates the realization of a bulk magnetic metamaterial by aggregating the R-NCs shown in figure 3.2g in a micro-channel evaporator[77] [78]. A slow evaporation of the solvent across a thin membrane drags a dilute suspension of R-NCs to the channel dead-end (Fig. 4.2a) and aggregates the particles into a dried 3D material[38], presenting a random, close-packed, isotropic nanostructure ((Figs. 4.2bc and 3.2g). The typical dimensions of a crack-free piece of metamaterial are 5 × 100 × 500 μm^3 gathering about 2.10^7 R-NCs for a filling fraction estimated at 40%.

Spectroscopic ellipsometry enabled the determination of the effective optical parameters reproduced in figures 4.2d-g, using the analysis method described in section 2.2 for semi-infinite materials. The electric permittivity and the magnetic permeability exhibit a resonant behavior around 400 nm, close to the free R-NC resonance (Fig. 3.2h). In particular, the real part μ' of the magnetic permeability explores values from 0.8 to 1.45.

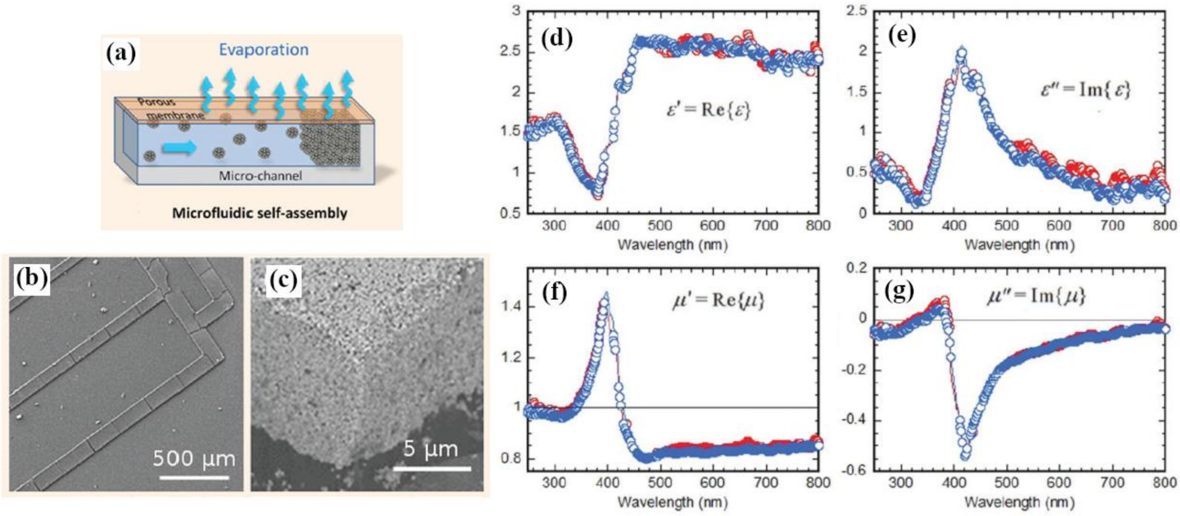

Figure 4.2: (a) Schematic view of the 3D assembly of R-NCs in a microfluidic evaporator. (b-c) SEM views of the assembled material at different magnification. (d-g) Experimental values of the complex electric permittivity ($\varepsilon'+i\varepsilon''$) and magnetic permeability ($\mu'+i\mu''$). Blue and red data points correspond to two different samples. (Reprinted from Ref. [38] with permission from The Royal Society of Chemistry).

This composite constitutes the first example of a 3D isotropic metamaterial exhibiting reflection properties consistent with an effective magnetic permeability significantly different from the natural value $\mu_r=1$ across the visible spectrum, and independent of the angle of incidence. This simple result however may hide the complexity of the magnetic behavior. The negative values of the imaginary part μ'' of the permeability for instance, reveals that the electric and magnetic responses are inextricably linked. The material is indeed dissipative if the electric and magnetic processes are considered together. Moreover, close to the resonance wavelength, some data points do not satisfy the linear relationship $Y=AX+B$ introduced in section 2, which denotes an angular variation of the coefficients A and B. This is a clear evidence of the phenomenon of spatial dispersion, which may preclude the extraction of valid effective optical parameters. Such theoretical limitations have been amply discussed in the literature[37,35,79,80]Finally, it should be noted that the full characterization of the optical parameters would require measurements of the reflected and transmitted waves, the latter being inaccessible yet.

-5- Conclusion

The various works reported in this chapter clearly demonstrate that the bottom-up approach brings a significant contribution to the design and generation of AOM and other properties. The main advantage of this approach is its ability to produce large amounts of magnetic meta-atoms, larger than the top-down techniques by several orders of magnitude. Moreover, the self-assembly techniques are generally cost-effective and energy saving as they do not require costly equipment such as electron beam lithography or ion-beam etching. The profusion of magnetic meta-atoms enables the production of metasurfaces of large area and of bulk magnetic materials of macroscopic size. They can be dispersed in aqueous or organic solvents to form “meta-inks” which can be conveniently implemented in various self-assembly techniques.

The newest plasmonic and all-dielectric designs provide magnetic and electric responses of equivalent magnitude, in narrow or broad frequency bands, opening the way to directional scattering. Scattering efficiencies significantly higher than 1 are obtained for typical sizes of order 100 to 200 nm, which is great for applications in monolayers in metasurfaces. The wavelength to diameter ratio however hardly exceeds 3 at resonance, which may not be optimal to warrant homogeneity. A trade-off has to be adjusted between homogeneity and efficiency: smaller sizes imply weaker optical response.

Disorder or inaccuracy, inherent of the bottom-up methods, are often seen as limitations for applications. It is true that the fabrication processes often result in some distribution of the sizes of the meta-atoms, implying variations of the optical properties. For applications requiring an accurate design, the usual methods of size-sorting of nanoparticles like centrifugation, viscosity gradient centrifugation[81], or gel electrophoresis[82] are available.

The self-organization of the meta-atoms may also lead to disordered materials, although monolayer of monodisperse spheres can self-organize in excellent triangular lattices as shown in figure 4.1. The relevant question is after all: what kind of order is required for a given application or property? For a 2D structure, certain types of correlated disorder, like hyper-uniformity may be just as good as a regular lattice[83,84]. Many questions related to the effect of disorder remain open that should be addressed in the future.

Finally, we note that the realization of 3D magnetic materials offers the unique opportunity to investigate experimentally the subtle and complex effects of non-locality and spatial dispersion and explore the limits of validity of an effective magnetic permeability parameter.

Acknowledgement:

The authors acknowledge the support of the LabEx AMADEus (ANR-10-LABX-42) in the framework of IdEx Bordeaux (ANR-10-IDEX-03-02), France

References:

---

[1] Landau, L. D., Lifshitz, E. M. (1960) Electrodynamics of Continuous Media, Pergamon Press, Oxford.

[2] Pendry, J. B., Holden, A. J., Robbins, D. J., & Stewart, W. J. (1999). Magnetism from conductors and enhanced nonlinear phenomena. *IEEE transactions on microwave theory and techniques*, *47*(11), 2075-2084.

[3] Smith, D. R., Padilla, W. J., Vier, D. C., Nemat-Nasser, S. C., & Schultz, S. (2000). Composite medium with simultaneously negative permeability and permittivity. *Physical review letters*, *84*(18), 4184.

[4] Shelby, R. A., Smith, D. R., & Schultz, S. (2001). Experimental verification of a negative index of refraction. *Science*, *292*(5514), 77-79.

---

[5] Soukoulis, C. M., & Wegener, M. (2011). Past achievements and future challenges in the development of three-dimensional photonic metamaterials. *Nature Photonics*, *5*(9), 523-530.

[6] Grigorenko, A. N., Geim, A. K., Gleeson, H. F., Zhang, Y., Firsov, A. A., Khrushchev, I. Y., & Petrovic, J. (2005). Nanofabricated media with negative permeability at visible frequencies. *Nature*, *438*(7066), 335-338.

[7] Dolling, G., Enkrich, C., Wegener, M., Zhou, J. F., Soukoulis, C. M., & Linden, S. (2005). Cut-wire pairs and plate pairs as magnetic atoms for optical metamaterials. *Optics letters*, *30*(23), 3198-3200.

[8] Linden, S., Enkrich, C., Wegener, M., Zhou, J., Koschny, T., & Soukoulis, C. M. (2004). Magnetic response of metamaterials at 100 terahertz. *Science*, *306*(5700), 1351-1353.

[9] Zhang, S., Fan, W., Panoiu, N. C., Malloy, K. J., Osgood, R. M., & Brueck, S. R. J. (2005). Experimental demonstration of near-infrared negative-index metamaterials. *Physical Review Letters*, 95(13), 137404.

[10] Dolling, G., Enkrich, C., Wegener, M., Soukoulis, C. M., & Linden, S. (2006). Simultaneous negative phase and group velocity of light in a metamaterial. *Science*, *312*(5775), 892-894.

[11] Chettiar, U. K., Kildishev, A. V., Yuan, H. K., Cai, W., Xiao, S., Drachev, V. P., & Shalaev, V. M. (2007). Dual-band negative index metamaterial: double negative at 813 nm and single negative at 772 nm. *Optics Letters*, *32*(12), 1671-1673.

[12] Jahani, S., & Jacob, Z. (2016). All-dielectric metamaterials. *Nature nanotechnology*, *11*(1), 23-36.

[13] Staude, I., Miroshnichenko, A. E., Decker, M., Fofang, N. T., Liu, S., Gonzales, E., ... & Kivshar, Y. (2013). Tailoring directional scattering through magnetic and electric resonances in subwavelength silicon nanodisks. *ACS nano*, *7*(9), 7824-7832.

[14] García-Meca, C., Hurtado, J., Martí, J., Martínez, A., Dickson, W., & Zayats, A. V. (2011). Low-loss multilayered metamaterial exhibiting a negative index of refraction at visible wavelengths. *Physical review letters*, *106*(6), 067402.

[15] Valentine, J., Zhang, S., Zentgraf, T., Ulin-Avila, E., Genov, D. A., Bartal, G., & Zhang, X. (2008). Three-dimensional optical metamaterial with a negative refractive index. *Nature*, *455*(7211), 376-379.

[16] Liu, N., Fu, L., Kaiser, S., Schweizer, H., & Giessen, H. (2008). Plasmonic building blocks for magnetic molecules in three-dimensional optical metamaterials. *Advanced Materials*, *20*(20), 3859-3865.

[17] Bohren, C. F., & Huffman, D. R. (2008). *Absorption and scattering of light by small particles*. John Wiley & Sons.

[18] Arbouet, A., Christofilos, D., Del Fatti, N., Vallée, F., Huntzinger, J. R., Arnaud, L., ... & Broyer, M. (2004). Direct measurement of the single-metal-cluster optical absorption. *Physical review letters*, *93*(12), 127401.

[19] Muskens, O. L., Bachelier, G., Fatti, N. D., Vallee, F., Brioude, A., Jiang, X., & Pileni, M. P. (2008). Quantitative absorption spectroscopy of a single gold nanorod. The Journal of Physical Chemistry C, 112(24), 8917-8921.

[20] Sheikholeslami, S. N., Alaeian, H., Koh, A. L., & Dionne, J. A. (2013). A metafluid exhibiting strong optical magnetism. *Nano letters*, *13*(9), 4137-4141.

[21] Ponsinet, V., Barois, P., Gali, S. M., Richetti, P., Salmon, J. B., Vallecchi, A., ... & Treguer-Delapierre, M. (2015). Resonant isotropic optical magnetism of plasmonic nanoclusters in visible light. *Physical Review B*, *92*(22), 220414.

[22] Elancheliyan, R., Dezert, R., Castano, S., Bentaleb, A., Nativ-Roth, E., Regev, O., Barois, P., Baron, A., Mondain-Monval, O., & Ponsinet, V. (2020). Tailored self-assembled nanocolloidal Huygens scatterers in the visible. Nanoscale, **12**(47), 24177-24187

[23] Many, V., Dézert, R., Duguet, E., Baron, A., Jangid, V., Ponsinet, V., ... & Tréguer-Delapierre, M. (2019). High optical magnetism of dodecahedral plasmonic meta-atoms. *Nanophotonics*, *8*(4), 549-558.

[24] Lermusiaux, L., Many, V., Barois, P., Ponsinet, V., Ravaine, S., Duguet, E., ... & Baron, A. (2021). Toward Huygens' Sources with Dodecahedral Plasmonic Clusters. *Nano Letters*.

[25] Smith, D. R., Padilla, W. J., Vier, D. C., Nemat-Nasser, S. C., & Schultz, S. (2000). Composite medium with simultaneously negative permeability and permittivity. Physical review letters, 84(18), 4184.

[26] Smith, D. R., Schultz, S., Markoš, P., & Soukoulis, C. M. (2002). Determination of effective permittivity and permeability of metamaterials from reflection and transmission coefficients. Physical review B, 65(19), 195104.

[27] Smith, D. R., Vier, D. C., Koschny, T., & Soukoulis, C. M. (2005). Electromagnetic parameter retrieval from inhomogeneous metamaterials. Physical review E, 71(3), 036617.

[28] Jackson, J.D. Classical electrodynamics, 3rd edition, 1998. John Wiley & Sons.

[29] Flamant, Q., Torrent, D., Gomez-Graña, S., Grigorenko, A. N., Kravets, V. G., Barois, P., ... & Baron, A. (2019). Direct retrieval method of the effective permittivity and permeability of bulk semi-infinite metamaterials by variable-angle spectroscopic ellipsometry. OSA Continuum, 2(5), 1762-1772.

[30] Shalaev, V. M., Cai, W., Chettiar, U. K., Yuan, H. K., Sarychev, A. K., Drachev, V. P., & Kildishev, A. V. (2005). Negative index of refraction in optical metamaterials. Optics letters, 30(24), 3356-3358

---

[31] Dolling, G., Enkrich, C., Wegener, M., Soukoulis, C. M., & Linden, S. (2006). Simultaneous negative phase and group velocity of light in a metamaterial. Science, 312(5775), 892-894.

[32] Dolling, G., Wegener, M., Soukoulis, C. M., & Linden, S. (2007). Negative-index metamaterial at 780 nm wavelength. Optics letters, 32(1), 53-55.

[33] Guth, N., Gallas, B., Rivory, J., Grand, J., Ourir, A., Guida, G., ... & De Rosny, J. (2012). Optical properties of metamaterials: Influence of electric multipoles, magnetoelectric coupling, and spatial dispersion. *Physical Review B*, *85*(11), 115138.

[34] Simovski, C. R. (2010). On electromagnetic characterization and homogenization of nanostructured metamaterials. *Journal of Optics*, *13*(1), 013001.

[35] *Nanostructured Metamaterials,*A.F. de Baas, S. Tretyakov, P. Barois *et al.*, Eds. Publications Office of the European Union (2010). ISBN 978-92-79-07563-6, doi 10.2777/54953. Available at: https://ec.europa.eu/research/industrial_technologies/pdf/metamaterials-brochure_en.pdf

[36] Menzel, C., Paul, T., Rockstuhl, C., Pertsch, T., Tretyakov, S., & Lederer, F. (2010). Validity of effective material parameters for optical fishnet metamaterials. *Physical Review B*, *81*(3), 035320.

[37] Alu, A. (2011). First-principles homogenization theory for periodic metamaterials. *Physical Review B*, *84*(7), 075153.

[38] Gómez-Graña, S., Le Beulze, A., Treguer-Delapierre, M., Mornet, S., Duguet, E., Grana, E., ... & Barois, P. (2016). Hierarchical self-assembly of a bulk metamaterial enables isotropic magnetic permeability at optical frequencies. *Materials Horizons*, *3*(6), 596-601.

[39] Monticone, F., & Alu, A. (2014). The quest for optical magnetism: from split-ring resonators to plasmonic nanoparticles and nanoclusters. *Journal of Materials Chemistry C*, *2*(43), 9059-9072.

[40] Alù, A., Salandrino, A., & Engheta, N. (2006). Negative effective permeability and left-handed materials at optical frequencies. *Optics express*, *14*(4), 1557-1567.

[41] Alù, A., & Engheta, N. (2008). Dynamical theory of artificial optical magnetism produced by rings of plasmonic nanoparticles. *Physical Review B*, *78*(8), 085112.

[42] Alu, A., & Engheta, N. (2009). The quest for magnetic plasmons at optical frequencies. *Optics express*, *17*(7), 5723-5730.

[43] Simovski, C. R., & Tretyakov, S. A. (2009). Model of isotropic resonant magnetism in the visible range based on core-shell clusters. *Physical Review B*, *79*(4), 045111.

[44] Vallecchi, A., Albani, M., & Capolino, F. (2011). Collective electric and magnetic plasmonic resonances in spherical nanoclusters. *Optics Express*, *19*(3), 2754-2772.

[45] Mühlig, S., Cunningham, A., Scheeler, S., Pacholski, C., Bürgi, T., Rockstuhl, C., & Lederer, F. (2011). Self-assembled plasmonic core–shell clusters with an isotropic magnetic dipole response in the visible range. *ACS nano*, *5*(8), 6586-6592.

[46] Qian, Z., Hastings, S. P., Li, C., Edward, B., McGinn, C. K., Engheta, N., ... & Park, S. J. (2015). Raspberry-like metamolecules exhibiting strong magnetic resonances. *ACS nano*, *9*(2), 1263-1270.

[47] Grillo, R., Beutel, D., Cataldi, U., Rockstuhl, C., & Bürgi, T. (2020). Self-Assembled Arrays of Gold Nanorod-Decorated Dielectric Microspheres with a Magnetic Dipole Response in the Visible Range for Perfect Lensing and Cloaking Applications. *ACS Applied Nano Materials*, *3*(6), 6108-6117.

[48] Fan, J. A., Wu, C., Bao, K., Bao, J., Bardhan, R., Halas, N. J., ... & Capasso, F. (2010). Self-assembled plasmonic nanoparticle clusters. *Science*, *328*(5982), 1135-1138.

[49] Roller, E. M., Khorashad, L. K., Fedoruk, M., Schreiber, R., Govorov, A. O., & Liedl, T. (2015). DNA-assembled nanoparticle rings exhibit electric and magnetic resonances at visible frequencies. *Nano letters*, *15*(2), 1368-1373.

[50] Fontana, J., Dressick, W. J., Phelps, J., Johnson, J. E., Rendell, R. W., Sampson, T., ... & Soto, C. M. (2014). Virus-templated Plasmonic nanoclusters with icosahedral symmetry via directed self-assembly. *Small*, *10*(15), 3058-3063.

[51] Désert, A., Chaduc, I., Fouilloux, S., Taveau, J. C., Lambert, O., Lansalot, M., ... & Duguet, E. (2012). High-yield preparation of polystyrene/silica clusters of controlled morphology. *Polymer Chemistry*, *3*(5), 1130-1132.

[52] Chomette, C., Tréguer-Delapierre, M., Schade, N. B., Manoharan, V. N., Lambert, O., Taveau, J. C., ... & Duguet, E. (2017). Colloidal alchemy: conversion of polystyrene nanoclusters into gold. *ChemNanoMat*, *3*(3), 160-163.

[53] Jahani, S., & Jacob, Z. (2016). All-dielectric metamaterials. *Nature nanotechnology*, *11*(1), 23-36.

[54] Baranov, D. G., Zuev, D. A., Lepeshov, S. I., Kotov, O. V., Krasnok, A. E., Evlyukhin, A. B., & Chichkov, B. N. (2017). All-dielectric nanophotonics: the quest for better materials and fabrication techniques. *Optica*, *4*(7), 814-825.

---

[55] Aspnes, D. E., & Studna, A. A. (1983). Dielectric functions and optical parameters of si, ge, gap, gaas, gasb, inp, inas, and insb from 1.5 to 6.0 ev. *Physical review B*, *27*(2), 985.

[56] Evlyukhin, A. B., Novikov, S. M., Zywietz, U., Eriksen, R. L., Reinhardt, C., Bozhevolnyi, S. I., & Chichkov, B. N. (2012). Demonstration of magnetic dipole resonances of dielectric nanospheres in the visible region. *Nano letters*, *12*(7), 3749-3755.

[57] Zywietz, U., Evlyukhin, A. B., Reinhardt, C., & Chichkov, B. N. (2014). Laser printing of silicon nanoparticles with resonant optical electric and magnetic responses. *Nature communications*, *5*(1), 1-7.

[58] De Marco, M. L., Semlali, S., Korgel, B. A., Barois, P., Drisko, G. L., & Aymonier, C. (2018). Silicon-Based Dielectric Metamaterials: Focus on the Current Synthetic Challenges. *Angewandte Chemie International Edition*, *57*(17), 4478-4498.

[59] Shi, L., Harris, J. T., Fenollosa, R., Rodriguez, I., Lu, X., Korgel, B. A., & Meseguer, F. (2013). Monodisperse silicon nanocavities and photonic crystals with magnetic response in the optical region. *Nature communications*, *4*(1), 1-7.

[60] Thiessen, A. N., Ha, M., Hooper, R. W., Yu, H., Oliynyk, A. O., Veinot, J. G., & Michaelis, V. K. (2019). Silicon nanoparticles: are they crystalline from the core to the surface?. *Chemistry of Materials*, *31*(3), 678-688.

[61] Chaâbani, W., Proust, J., Movsesyan, A., Béal, J., Baudrion, A. L., Adam, P. M., ... & Plain, J. (2019). Large-scale and low-cost fabrication of silicon mie resonators. *ACS nano*, *13*(4), 4199-4208.

[62] Hinamoto, T., Hotta, S., Sugimoto, H., & Fujii, M. (2020). Colloidal Solutions of Silicon Nanospheres toward All-Dielectric Optical Metafluids. *Nano Letters*, *20*(10), 7737-7743.

[63] Dezert, R., Richetti, P., & Baron, A. (2019). Complete multipolar description of reflection and transmission across a metasurface for perfect absorption of light. *Optics express*, *27*(19), 26317-26330.

[64] Liu, W., Miroshnichenko, A. E., Neshev, D. N., & Kivshar, Y. S. (2012). Broadband unidirectional scattering by magneto-electric core–shell nanoparticles. *ACS nano*, *6*(6), 5489-5497.

[65] Tsuchimoto, Y., Yano, T. A., Hayashi, T., & Hara, M. (2016). Fano resonant all-dielectric core/shell nanoparticles with ultrahigh scattering directionality in the visible region. *Optics express*, *24*(13), 14451-14462.

[66] De Marco, M. L., Jiang, T., Fang, J., Lacomme, S., Zheng, Y., Baron, A., ... & Aymonier, C. (2021). Broadband Forward Light Scattering by Architectural Design of Core–Shell Silicon Particles. *Advanced Functional Materials*, 2100915.

[67] Rockstuhl, C., Lederer, F., Etrich, C., Pertsch, T., & Scharf, T. (2007). Design of an artificial three-dimensional composite metamaterial with magnetic resonances in the visible range of the electromagnetic spectrum. *Physical review letters*, *99*(1), 017401.

[68] Bourgeois, M. R., Liu, A. T., Ross, M. B., Berlin, J. M., & Schatz, G. C. (2017). Self-Assembled plasmonic metamolecules exhibiting tunable magnetic response at optical frequencies. *The Journal of Physical Chemistry C*, *121*(29), 15915-15921.

[69] Dintinger, J., Mühlig, S., Rockstuhl, C., & Scharf, T. (2012). A bottom-up approach to fabricate optical metamaterials by self-assembled metallic nanoparticles. *Optical Materials Express*, *2*(3), 269-278.

[70] Dezert, R., Richetti, P., & Baron, A. (2017). Isotropic Huygens dipoles and multipoles with colloidal particles. *Physical Review B*, *96*(18), 180201.

[71] Glybovski, S. B., Tretyakov, S. A., Belov, P. A., Kivshar, Y. S., & Simovski, C. R. (2016). Metasurfaces: From microwaves to visible. *Physics reports*, *634*, 1-72.

[72] Pichumani, M., Bagheri, P., Poduska, K. M., González-Viñas, W., & Yethiraj, A. (2013). Dynamics, crystallization and structures in colloid spin coating. *Soft Matter*, *9*(12), 3220-3229.

[73] Berteloot, G., Daerr, A., Lequeux, F., & Limat, L. (2013). Dip coating with colloids and evaporation. *Chemical Engineering and Processing: Process Intensification*, 68, 69-73.

[74] Yang, H., & Jiang, P. (2010). Large-scale colloidal self-assembly by doctor blade coating. Langmuir, 26(16), 13173-13182.

[75] Meldrum, F. C., Kotov, N. A., & Fendler, J. H. (1994). Utilization of surfactant-stabilized colloidal silver nanocrystallites in the construction of mono-and multiparticulate Langmuir-Blodgett films. *Langmuir*, *10*(7), 2035-2040.

[76] Malassis, L., Massé, P., Tréguer-Delapierre, M., Mornet, S., Weisbecker, P., Kravets, V., ... & Barois, P. (2013). Bottom-up fabrication and optical characterization of dense films of meta-atoms made of core–shell plasmonic nanoparticles. *Langmuir*, *29*(5), 1551-1561.

[77] Leng, J., Lonetti, B., Tabeling, P., Joanicot, M., & Ajdari, A. (2006). Microevaporators for kinetic exploration of phase diagrams. *Physical review letters*, *96*(8), 084503.

---

[78] Angly, J., Iazzolino, A., Salmon, J. B., Leng, J., Chandran, S. P., Ponsinet, V., ... & Correa-Duarte, M. A. (2013). Microfluidic-induced growth and shape-up of three-dimensional extended arrays of densely packed nanoparticles. *ACS nano*, *7*(8), 6465-6477.

[79] Simovski, C. R., & Tretyakov, S. (2009). Material parameters and field energy in reciprocal composite media. Theory and Phenomena of Metamaterials, ed F Capolino.

[80] Agranovich, V. M., & Ginzburg, V. (2013). *Crystal optics with spatial dispersion, and excitons* (Vol. 42). Springer Science & Business Media.

[81] Qiu, P., & Mao, C. (2011). Viscosity gradient as a novel mechanism for the centrifugation-based separation of nanoparticles. *Advanced Materials*, *23*(42), 4880-4885.

[82] Surugau, N., & Urban, P. L. (2009). Electrophoretic methods for separation of nanoparticles. *Journal of separation science*, *32*(11), 1889-1906.

[83] Torquato, S., & Stillinger, F. H. (2003). Local density fluctuations, hyperuniformity, and order metrics. *Physical Review E*, *68*(4), 041113.

[84] Leseur, O., Pierrat, R., & Carminati, R. (2016). High-density hyperuniform materials can be transparent. *Optica*, *3*(7), 763-767.